PAPER

Check for updates

Novel efficient deep-red emitting phosphor SrCa₂Ga₂O₆:Mn⁴⁺ with tululite-related structure†

Wataru Hikita, [ID] [a] Masato Iwaki, [ID] [a] Mizuki Watanabe,[a] Kazuyoshi Uematsu,[b] Mineo Sato[b] and Kenji Toda*[a]

Mn⁴⁺-activated phosphors have been attracted to replace the rare-earth-activated phosphors in the use of deep-red optical devices. Owing to their low toxicity and wide applications, oxide materials are promising hosts for Mn⁴⁺ phosphors. Exploration into novel oxides is important for developing new Mn⁴⁺-doped phosphors with high luminescent efficiencies. In this study, we discovered the deep-red emitting phosphor SrCa₂Ga₂O₆:Mn⁴⁺ in the Sr₃Ga₂O₆–Ca₃Ga₂O₆ solid solution system. From the single crystal X-ray diffraction analysis, SrCa₂Ga₂O₆:Mn⁴⁺ was found to crystallize in a cubic unit cell with space group *F*432. Furthermore, SrCa₂Ga₂O₆:Mn⁴⁺ was revealed to be a new member of tululite structure-related phosphors, such as Ca₁₄Zn₆Al₁₀O₃₅:Mn⁴⁺, Ca₁₄Zn₆Ga₁₀O₃₅:Mn⁴⁺, and Ca₁₄Mg₄Ga₁₂O₃₆:Mn⁴⁺. To study the fundamental luminescence properties, we synthesized SrCa₂Ga₂O₆:Mn⁴⁺ powder samples *via* the conventional solid-state reaction method. SrCa₂Ga₂O₆:Mn⁴⁺ has an absorption band in the region of 250–550 nm, and shows a deep-red emission band peaks at 712 nm. The excitation band is well matched to the emission wavelength of near-ultraviolet and blue light emitting diodes. The optimized sample exhibited high quantum efficiency and good thermal quenching properties. This study revealed SrCa₂Ga₂O₆:Mn⁴⁺ has excellent potential as a deep-red emitting phosphor and is expected to be used for commercial applications, such as indoor plant cultivation and wavelength down-convertor for solar-cells.

Introduction

Tetravalent manganese ion (Mn⁴⁺)-activated phosphors are well known for deep-red emission in the wavelength range of 600 to 760 nm under near-ultraviolet (n-UV) or blue light excitation (250–550 nm).[1-3] The major applications of these phosphors are solid-state lighting, indoor plant cultivation, and wavelength down-convertors for solar cells.[4-9] Moreover, Mn⁴⁺-activated phosphors are considered to replace the major rare-earth (Eu³⁺, Eu²⁺, and Ce³⁺)-activated red-emitting phosphors due to their lower cost and longer emission wavelength.[10-13] Therefore, Mn⁴⁺ takes an important role as a luminescent center in phosphors.

The most common host materials for Mn⁴⁺-doped phosphors are fluorides or oxides. Fluoride-based phosphors, such as K₂SiF₆:Mn⁴⁺ and K₂TiF₆:Mn⁴⁺, have been used as red components for optical devices like light-emitting diodes (w-LEDs). They show narrow band emission peak at

approximately 630 nm with high quantum efficiencies (80–90%).[14-16] However, fluoride phosphors have some problems, such as the use of highly toxic material HF in synthesis and low physical and chemical stability.[17,18] In addition, their short emission wavelength and narrow spectrum are not suitable for applications like artificial plant growth, which requires deep-red emission in the 650–750 nm range.[19] On the other hand, Mn⁴⁺-activated oxide phosphors typically exhibit deep-red broad emission peaking between 650 and 760 nm. Furthermore, they can be synthesized easier and safer than fluoride phosphors.[1] The stronger covalency of Mn⁴⁺–O²⁻ bonds compared to Mn⁴⁺–F⁻ provide longer emission wavelength, which can fulfill the demands of indoor plant cultivation and wavelength down-converter for solar cells.[20] From the both safety and practical perspectives, oxide hosts are favorable.

To improve the luminescence properties of Mn⁴⁺-doped phosphors, host lattice tuning by doping with different cations is generally considered. This approach can stabilize the Mn ion as tetravalent, cause structural distortion, and sensitize Mn⁴⁺ by energy transfer phenomenon.[21-24] However, significant improvements to reach practical use are difficult in many cases. Thus, it is desirable to select phosphors with good luminescence properties as the starting materials. Based on these considerations, we focused on exploring novel oxide materials suitable as Mn⁴⁺ phosphors.

*a*Graduate School of Science and Technology, Niigata University, 8050 Ikarashi 2-no-cho, Niigata 950-2181, Japan. E-mail: ktoda@eng.niigata-u.ac.jp; Fax: +81 025-262-6771; Tel: +81 025-262-6771

*b*Department of Chemistry and Chemical Engineering, Faculty of Engineering, Niigata University, Ikarashi 2-no-cho, Niigata City, 950-2181, Japan

We have been searching for new materials suitable as phosphor hosts. For instance, we previously reported the Ba_6-$La_2Al_{1.5}Fe_{2.5}O_{15}$-type green-emitting phosphor $Ba_5La_3MgAl_3$-O_{15}:Ce^{3+} and the Olivine-type red-emitting phosphor $NaMgPO_4$:Eu^{2+}.[25,26] Similarly, Singh *et al.* discovered the red-emitting phosphor $Li_3RbGe_8O_{18}$:Mn^{4+} with a novel crystal structure by a combinatorial synthesis within the $A_2Ge_4O_9$ (A = Li, K, and Rb) series.[5] Among these compounds, Li_3RbGe_8-O_{18}:Mn^{4+} displayed the highest emission intensity, which is a successful example of material discovery. These examples highlight that searching for novel host materials is effective.

In this study, we selected gallate compounds as potential host materials for Mn^{4+}-activated phosphors. For instance of gallate-based Mn^{4+}-doped phosphors, $Ca_{14}Zn_6Ga_{10}O_{35}$:Mn^{4+}, $Mg_7GeGa_2O_{12}$:Mn^{4+}, $Mg_6ZnGeGa_2O_{12}$:Mn^{4+}, $Mg_3GeGa_2O_8$:Mn^{4+}, $LaGaO_3$:Mn^{4+}, $SrLaGaO_4$:Mn^{4+}, $SrLaGa_3O_7$:Mn^{4+}, and $Ca_{14}Mg_4Ga_{12}O_{36}$:Mn^{4+} ($Ca_7Mg_2Ga_6O_{18}$:Mn^{4+}) have been previously reported.[27–34] Gallate compounds often make $[GaO_6]$ octahedra in these crystal lattices, which are essential for Mn^{4+}-activated phosphors because Mn^{4+} can display its characteristic emission when placed in a six-fold octahedral coordination environment. Consequently, Mn^{4+}-doped gallate phosphors have been widely studied. In this work, we aimed to discover novel compounds in oxide systems containing Ga_2O_3.

As a result, we successfully discovered a deep-red-emitting phosphor with the empirical formula $SrCa_2Ga_2O_6$:Mn^{4+} in the $Sr_3Ga_2O_6$–$Ca_3Ga_2O_6$ solid solution system. $SrCa_2Ga_2O_6$:Mn^{4+} exhibits a broad absorption band from n-UV to blue light (250–500 nm) and shows intense deep-red emission peaks at 712 nm. However, due to the unknown crystal structure of $SrCa_2Ga_2$-O_6:Mn^{4+}, its luminescence mechanism is unidentified. To clarify the crystal structure, a single crystal X-ray diffraction analysis was performed. Herein, we report the crystal structure of the novel deep-red emitting phosphor $SrCa_2Ga_2O_6$:Mn^{4+} and its fundamental luminescence properties.

Experimental section

Materials and synthesis methods

$SrCa_2Ga_2O_6$:Mn^{4+} (SCG:Mn^{4+}) single crystals were synthesized by a flux method. $SrCO_3$ (Kanto Chemical Co., Inc, 99.9%), $CaCO_3$ (Kanto Chemical Co., Inc, 99.99%), Ga_2O_3 (Kojundo Chemical Lab., 99.99%), and MnO_2 (Wako Pure Chemical Co., 99.5%) were weighed in a stoichiometric ratio of Sr : Ca : Ga : Mn = 1 : 2 : 1.99 : 0.01. The raw materials were mixed with acetone in an agate mortar. After drying, 50 wt% of prepared weight of $SrCl_2$ (Kojundo Chemical Lab., 99.9%) was added to the agate mortar as flux and re-mixed without solvent. The homogeneously mixed powder was mounted on an alumina boat, calcined at 1473 K for 6 h in ambient air, then cooled to 1123 K at 50 K h^{-1}, and finally natural-cooled to ambient temperature. The yellow single crystals produced on the alumina boat were separated using a spatula.

$SrCa_2Ga_{2(1-x)}Mn_{2x}O_6$ ($0 \leq x \leq 0.07$) powders were synthesized by a conventional solid-state reaction method. The same raw materials except $SrCl_2$ flux were mixed using the agate mortar in a stoichiometric ratio of Sr : Ca : Ga : Mn = 1 : 2 : 2(1 − x) : 2x ($0 \leq$ $x \leq 0.07$). The mixture was mounted on the alumina boat and heated at 1473 K for 6 h in ambient air. The sintered samples were ground with agate mortar for several characterizations.

Characterization

The crystallographic data of SCG:Mn^{4+} were collected for the single crystal X-ray diffraction (XRD). A single crystal was put on a glass capillary. The XRD data were measured using a single crystal X-ray diffractometer XtaLAB mini (Rigaku). Data collection, cell refinement, and data reduction were computed using the Crystal Clear-SM Auto 2.0 rl (Rigaku, 2009). The structural analysis was performed using a structural analysis software CrystalStructure 4.3 (Rigaku, 2019). The initial structure was obtained by a direct method using SIR2008.[35] The structural parameters were refined using the SHELXL2014 program.[36] The refined structural data was re-performed by a structural analysis software WinGX for twin refinement.[37] The VESTA program was used to visualize the crystal structure.[38] The semiquantitative measurement of the carbon-coated single crystal samples was performed using an electron probe microanalyzer EPMA-1720 (Shimadzu).

The XRD patterns of the powder samples were obtained using an X-ray diffractometer MiniFlex-600 (Rigaku) with a monochromatic Cu Kα radiation ($\lambda = 1.54056$ Å) under 10 mA and 30 kV. The XRD data for the Rietveld refinement were collected using an X-ray diffractometer D2 PHASER (Bruker) with a monochromatic Cu Kα radiation ($\lambda = 1.54056$ Å) under 10 mA and 30 kV. Rietveld refinement was carried out using the REITAN-FP program software.[39] The major elements in the powders were determined by X-ray fluorescence (XRF) spectroscopy using an XRF spectrometer SEA1200VX (SII Nano Technology). The reflection and absorption spectra of the powder samples were measured using a UV-visible spectrometer V-750 (JASCO) based on $BaSO_4$ white ceramics as a reference and were evaluated using a diffuse reflectance spectrum. The particle morphology of powder samples was observed using a scanning electron microscope (SEM) JSM-IT200 (JEOL). Photoluminescence (PL) and photoluminescence excitation (PLE) spectra were obtained using a spectrofluorometer FP-6500/FP-6600 (JASCO) with a 150 W Xenon lamp at 298 K. Near-infrared (NIR) photoluminescence was measured using a spectrometer RB4524-NIRC3 (OtO photonics) with an attached CCD detector. Absolute quantum efficiency was measured using an integrating sphere ISF-834 (JASCO) with a photoluminescence spectrometer FP-8500 (JASCO), and a standard halogen lamp ESC-842 (JASCO) was used for calibration of the measurement system. The PL decay curves were measured using the Quantaurus-tau (Hamamatsu Photonics). Thermal quenching PL spectra was measured using a PL equipment (FP-6500/FP-6600) with a heating attachment HPC-503 (JASCO).

Results and discussion

Crystal structure

The crystal structure of SCG:Mn^{4+} is illustrated in Fig. 1. SCG:Mn^{4+} crystallized in space group $F432$ (#209) with a cubic
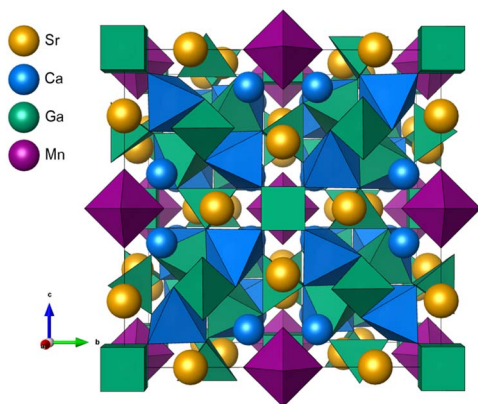
Fig. 1 The overview of refined crystal structure of $SrCa_2Ga_2O_6:Mn^{4+}$.

Table 1 Crystallographic data of the $SrCa_2Ga_{1.87}Mn_{0.13}O_6$ single crystal

Chemical formula	$SrCa_2Ga_{1.87}Mn_{0.13}O_6$
Formula weight (g mol^{-1})	401.26
Crystal system	Cubic
Space group	$F432$ (#209)
Measurement temperature (K)	296(2)
a (Å)	15.4894(15)
V (Å^3)	3716.2(11)
Z	24
Density (g cm^{-3})	4.303
Radiation type and wavelength (Å)	Mo Kα 0.71075
μ (mm^{-1})	18.54
Crystal size (mm^3)	$0.109 \times 0.094 \times 0.091$
Diffractometer	Rigaku XtaLAB mini
Absorption correction	Numerical (NUMABS; Rigaku, 1999)
T_{min}, T_{max}	1, 1
Measd, indep, obsd [$I > 2\sigma(I)$] reflns	6448, 377, 377
R [$F^2 > 2\sigma(F^2)$], $wR(F^2)$, S	0.0317, 0.0795, 1.272
$\Delta\rho_{max}$, $\Delta\rho_{min}$ (e Å^{-3})	1.25, -0.71
Absolute structure parameter	0.15(8)

unit cell with $a = 15.4894(15)$ Å, and the composition formula was determined to $SrCa_2Ga_{1.87}Mn_{0.13}O_6$. The detailed crystallographic data and atomic refinement parameters are listed in Tables 1 and 2. SCG:Mn^{4+} is a new member of tululite structure-related compounds ($Ca_{14}Zn_6Al_{10}O_{35}$, $Ca_{14}Zn_6Ga_{10}O_{35}$, $Ca_7Mg_2Ga_6O_{18}$, $Ca_7Co_3Ga_5O_{18}$, $Ca_{6.3}Mn_3Ga_{4.4}Al_{1.3}O_{18}$, and $Ca_7Mn_{2.14}Ga_{5.86}O_{17.93}$).[34,40–46] Notably, SCG:Mn^{4+} is the first material containing high-concentration strontium in the aforementioned series. The compositional identity between SCG and other materials with a fundamental formula $[A^{2+}_7][B^{2+}_2]\{C^{3+}_6\}O_{18}$ can be described to rewrite $SrCa_2Ga_2O_6$ as $[Sr_3Ca_4](Ca_2)\{Ga_6\}O_{18}$.

The cation-centered polyhedra in SCG:Mn^{4+} are shown in Fig. 2. There are 11 crystallographically independent sites (one strontium, two calcium, three gallium and four oxygen, and one gallium disordered with manganese). The Sr1 atom is coordinated by nine O atoms and forms a monocapped polyhedron.

The average bond length of Sr1–O is 2.6335 Å. Considering the 0.5 occupancy of the O4 atom, [Sr1O$_9$] is a virtually seven-coordinated prism. The Ca1 atom is coordinated by six O atoms and forms a distorted octahedron. The average bond length for Ca1–O is 2.3849 Å. The Ca2 atom is coordinated by five O atoms and forms a trigonal bipyramidal. The average bond length for Ca2–O is 2.1885 Å. Ga2 and Ga3 are coordinated by four O atoms and form tetrahedra. The Ga4 is coordinated by eight O atoms with 0.5 occupancy and composes a cubic structure. Considering Ga^{3+} cannot make eight-coordinated configuration, [Ga4O$_8$] is virtually four-coordinated tetrahedron. The average bond lengths for Ga2, Ga3, and Ga4 are 2.0610 Å, 1.8443 Å, and 1.8270 Å, respectively. The Ga1/Mn1 is coordinated by six O atoms and forms an octahedron, and its occupancy ratio is determined to 0.21(8)/0.79(8) for Ga1/Mn1. The average bond distance for (Ga1/Mn1)–O is 1.9424 Å. The introduction of Mn^{4+} ions into octahedral sites results in red emission.[47,48] Therefore, the deep-red emission of the single crystal was observed, as shown in Fig. S1.†

As shown in Fig. 3a, the tetrahedral structure is composed of [Ca2O$_5$], [Ga2O$_4$], [Ga3O$_4$], and [Ga4O$_8$] polyhedra via a vertex-sharing connection. [Ca2O$_5$] and [Ga2O$_4$] polyhedra with 0.5 occupancy formed cluster centered on the O2. [Ca2O$_5$] is connected to [Ga3O$_4$] and [Ga4O$_8$]. On the other hand, [Ga2O$_4$] is only connected to [Ga3O$_4$]. As shown in Fig. 3b, the octahedral cluster of [Ca1O$_6$] and [Sr1O$_9$] centered on the [(Ga1/Mn1)O$_4$] octahedron is also present, containing an aristotype perovskite-like structure (Fig. 3c). [Ca1O$_6$] is connected to [Sr1O$_9$] and [(Ga1/Mn1)O$_6$] via an edge-sharing. In contrast, [Sr1O$_9$] and [(Ga1/Mn1)O$_6$] are connected via the vertex-sharing. The crystal structure of SCG is constructed in the way that octahedral fragments filled the voids in the framework formed by the tetrahedral fragments with [Ga4O$_8$] cube as a vertex. On the SCG as a host, the complex structure isolates Mn^{4+} ions, and the long lattice separates octahedral sites, which is expected to protect Mn^{4+} ions from nonradiative perturbations.[49]

XRD measurements

The XRD patterns of $SrCa_2Ga_{2(1-x)}Mn_{2x}O_6$ ($0 \leq x \leq 0.07$) powders were measured, as shown in Fig. 4a. Most of the diffraction peaks are good agreement with simulation pattern calculated from the SCG:Mn^{4+} single crystal data. The undesirable peaks indexed to $Sr_3Ga_2O_6$ and $Ca_5Ga_6O_{14}$ are also detected. To confirm the crystal structure and phase purity, the Rietveld refinement was performed. Fig. 4b depicts the Rietveld refinement result for SCG:0.03Mn^{4+} powder using the SCG:Mn^{4+} single crystal structure data as a model. The crystallographic data and refined parameters of SCG:0.03Mn^{4+} are summarized in Tables S2 and S3.† The Mn^{4+} concentration in the SCG:0.03Mn^{4+} phase was fixed at 0.03 and all isotropic displacement parameters (B_{eq}) were fixed at 1.000. The R factors converged to $R_{wp} = 9.316$, $R_p = 6.556$, $R_e = 3.705$, and $S = 2.515$, indicating that the obtained result is reliable. The refined crystal structure is in good agreement with that of the single crystal data. $Sr_3Ga_2O_6$ and $Ca_5Ga_6O_{14}$ phases were successfully detected as impurities. The phase purity was found to be

Table 2 Atomic positions, occupancies, and anisotropic displacement parameters for the $SrCa_2Ga_{1.87}Mn_{0.13}O_6$ single crystal

Atom	Site	Occ.[a]	x	y	z	U_{ani} (Å^2)
Sr1	24e	1	0.20879(8)	1	0	0.0134(4)
Ca1	32f	1	0.38960(8)	0.88960(8)	0.11040(8)	0.0068(5)
Ca2	32f	0.5	0.1564(4)	0.8436(4)	0.1564(4)	0.031(2)
Ga1/Mn1	4b	0.20(8)/0.80(8)	0.5	1	0	0.0037(16)
Ga2	32f	0.5	0.17737(17)	0.82263(17)	0.17737(17)	0.0172(9)
Ga3	24d	1	0.25	1	0.25	0.0139(4)
Ga4	4a	1	0	1	0	0.0136(8)
O1	24e	1	0.3746(6)	1	0	0.0077(17)
O2	8c	1	0.25	0.75	0.25	0.027(4)
O3	96j	1	0.2509(6)	0.9334(6)	0.1513(4)	0.033(2)
O4	32f	0.5	0.0681(6)	0.9319(6)	0.0681(6)	0.017(4)

[a] Occ. means occupancy.
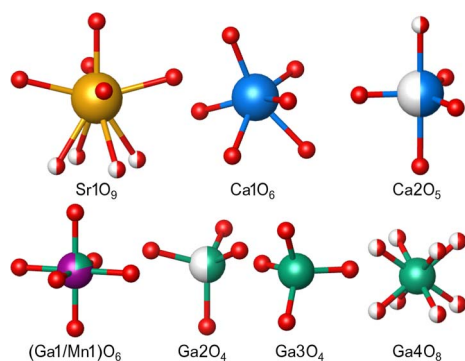
Fig. 2 Cation-centered polyhedra in $SrCa_2Ga_2O_6:Mn^{4+}$.
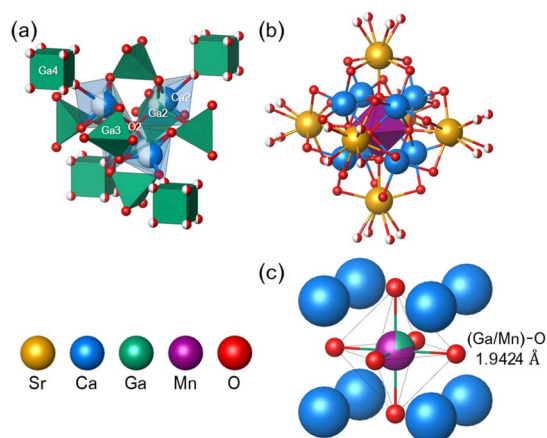
Fig. 3 (a) The tetrahedral cluster constructed by $[Ga2O_4]$, $[Ca2O_5]$, $[Ga3O_4]$, and $[Ga4O_8]$ centered on O2. (b) The octahedral cluster formed by $[Sr1O_9]$ and $[Ca1O_6]$ centered on $[(Ga1/Mn1)O_6]$ octahedron. (c) The aristotype perovskite-like structure composed of Ga1/Mn1, Ca1, and O1.

$SCG:0.03Mn^{4+} : Sr_3Ga_2O_6 : Ca_5Ga_6O_{14} = 93.74 : 0.40 : 5.86$ in mass%. These impurities may affect the luminescence properties because they have the tetrahedral sites where Mn^{5+} ions could substitute. To suppress the production of these impurities is difficult because they were probably produced from charge imbalance by replacing Ga^{3+} ion to Mn^{4+} ion and

compositional deviation from undesirable cation mixing of Sr^{2+} and Ca^{2+} ions. Therefore, in this study, we considered these impurities not affect the emission spectrum since they have no octahedral sites where Mn^{4+} ions can substitute. The XRF analysis was also performed to investigate the elements composed of the $SCG:Mn^{4+}$ powder (Table S4†). The elemental amount was in good agreement with the stoichiometric ratio. In this study, $SCG:Mn^{4+}$ powders were successfully synthesized.

UV-vis diffuse reflectance spectra

The UV-vis diffuse reflectance spectra of the SCG host powder and $SCG:0.03Mn^{4+}$ were measured (Fig. 5). In the SCG host powder, the reflection intensity between 300 and 800 nm is higher than 85%; thus, the host material has a white body color. To determine an energy band gap (E_g) of the non-doped SCG, a Kubelka–Munk formula (eqn (1)) was used;[50,51]

$$(\alpha h\nu)^{\frac{1}{2}} = \frac{K}{S} = \frac{(1-R)^2}{2R} \tag{1}$$

where h is a Plank's constant, ν is a frequency of light, K is an absorption coefficient, S is a scattering coefficient, and R is a reflectivity. By the Kubelka–Munk equation, the E_g is determined to be 4.89 eV, which is sufficiently large. On host materials with a large band gap, the interaction between the energy transition of Mn^{4+} and valence/conduction bands becomes less, and Mn^{4+} functions as an emission center.[52] In the $SCG:0.03Mn^{4+}$ powder, n-UV and blue light absorptions are clearly observed between 290 and 530 nm; hence, the body color of Mn^{4+}-doped SCG powder is yellow. The characteristic absorption spectrum indicates that Mn^{4+} ions occupy octahedral sites. On the other hand, an absorption band from 500 to 800 nm was also observed. This absorption is mainly due to the $^3A_2 \rightarrow {}^3T_1$ spin-allowed transition of Mn^{5+} in tetrahedral coordination environments, which overlaps with the emission of Mn^{4+}. Thus, a decrease in luminescence efficiency is anticipated due to the energy transfer from Mn^{4+} to Mn^{5+}.

PL properties

Fig. 6a shows the normalized PL and PLE spectra of the $SCG:0.03Mn^{4+}$ powder monitored at $\lambda_{ex} = 353$ nm and $\lambda_{em} =$

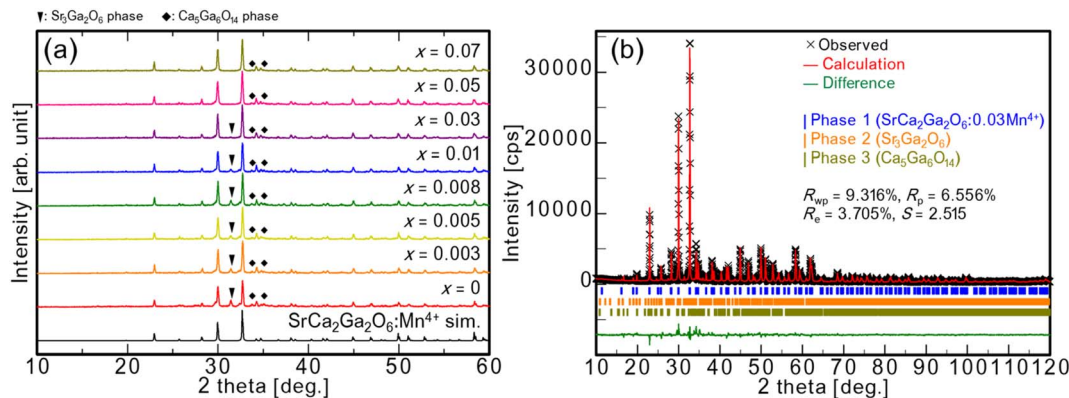**Fig. 4** (a) XRD patterns of SrCa$_2$Ga$_2$O$_6$:xMn^{4+} (0 ≤ x ≤ 0.07) powders. (b) Rietveld refinement result for XRD pattern of the SrCa$_2$Ga$_2$O$_6$:0.03Mn^{4+} sample.
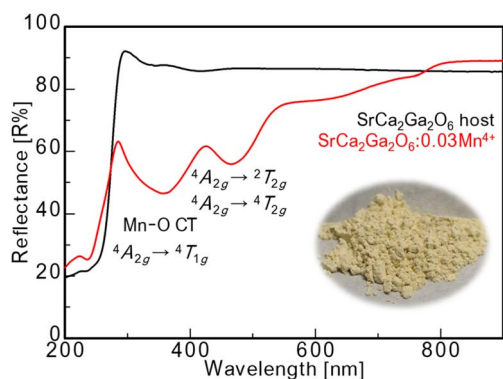
Fig. 5 UV-vis diffuse reflectance spectra of SrCa$_2$Ga$_2$O$_6$ (black) and SrCa$_2$Ga$_2$O$_6$:0.03Mn^{4+} (red). The insert photograph is the body color of SrCa$_2$Ga$_2$O$_6$:0.03Mn^{4+} under fluorescent light.

712 nm. PL and PLE spectra of SrCa$_2$Ga$_{2(1-x)}$Mn$_{2x}$O$_6$ (0.003 ≤ x ≤ 0.07) powders are also displayed in Fig. 6b. SCG:Mn^{4+} phosphors have a broad excitation band ranging from 250 to 550 nm. The emission spectrum peaked at 712 nm is observed, corresponding to ^{2}E$_g$ → ^{4}A$_{2g}$ spin-forbidden transition of Mn^{4+}. The PL measurement shows that the Mn^{4+} are successfully doped in octahedral sites. The optimal Mn^{4+} concentration is found to be x = 0.03, as shown in Fig. 6c. Moreover, the internal and external quantum efficiencies (QEs) of SCG:0.03Mn^{4+} under 365 nm excitation are 66% and 50%, and the absorbance is 76%. The QEs of SCG:0.03Mn^{4+} and other Mn^{4+}-activated gallate compounds are listed in Table 3. SCG:0.03Mn^{4+} exhibits sufficiently high quantum efficiencies, and its emission intensity is almost comparable with Ca$_{14}$Zn$_6$Ga$_{10}$O$_{35}$:Mn^{4+} (Fig. S3†).

The high symmetrical octahedral site increases the covalent bond strength between Mn^{4+} and ligands, and the strong covalent binding for the Mn^{4+}-ligand realizes deep-red emission by decreasing ^{2}E$_g$ → ^{4}A$_{2g}$ transition energy.[53,54] To consider the symmetry, a distortion index D was calculated using the following eqn (2);[55]

$$D = \frac{1}{n}\sum_{i=1}^{n}\frac{|d_i - d_{av}|}{d_{av}} \qquad (2)$$

where n is the coordination number, d_i is the bond length between the central atom and ith coordinating atom, d_{av} is the average bond length. For the SCG:Mn^{4+} single crystal, all the bond lengths of [(Ga1/Mn1)O$_6$] octahedron are 1.942(10) Å, and the D is 0. Therefore, SCG:Mn^{4+} powders display the emission topped at 712 nm. The nephelauxetic effect that affect the covalency is discussed in Crystal Field Analysis and Nephelauxetic Effect Calculation section.

The excitation spectra deconvolution of SCG:0.03Mn^{4+} was also conducted, as shown in Fig. 6d. As a result, the excitation band was successfully deconvoluted into four components with Mn^{4+}–O^{2-} charge transfer (CT) transition (centered at 34 293 cm^{-1} and 292 nm), ^{4}A$_{2g}$ → ^{4}T$_{1g}$ spin-allowed transition (centered at 27 896 cm^{-1} and 358 nm), ^{4}A$_{2g}$ → ^{2}T$_{2g}$ spin-forbidden transition (centered at 22 208 cm^{-1} and 450 nm), and ^{4}A$_{2g}$ → ^{4}T$_{2g}$ spin-allowed transition (centered at 20 578 cm^{-1} and 486 nm). These characteristic excitation peaks are well matched to n-UV and blue LED chips. The spectral change of excitation bands, as shown in Fig. 6b, is caused by the change of intensity ratio between CT transition and ^{4}A$_{2g}$ → ^{4}T$_{1g}$ transition.

To study the mechanism of concentration quenching, the luminescence lifetime measurement was conducted. The PL decay curves of SrCa$_2$Ga$_{2(1-x)}$Mn$_{2x}$O$_6$ (0.005 ≤ x ≤ 0.07) powders are shown in Fig. 7. The luminescence lifetimes are calculated using the following first-order exponential decay model (eqn (3)) because the Mn^{4+} ion occupies one Ga^{3+} octahedral coordination environment in SCG:Mn^{4+};[57]

$$I(t) = I_1(0)\exp\left(-\frac{t}{\tau_1}\right) \qquad (3)$$

where $I(t)$ is the emission intensity at time t, $I_1(0)$ is the initial emission intensity, t is the time, τ_1 is the luminescence lifetime. However, the double-order decay model (eqn (4)) can also be applied to high Mn^{4+} concentration samples;[58]

$$I(t) = I_1(0)\exp\left(-\frac{t}{\tau_1}\right) + I_2(0)\exp\left(-\frac{t}{\tau_2}\right) \qquad (4)$$

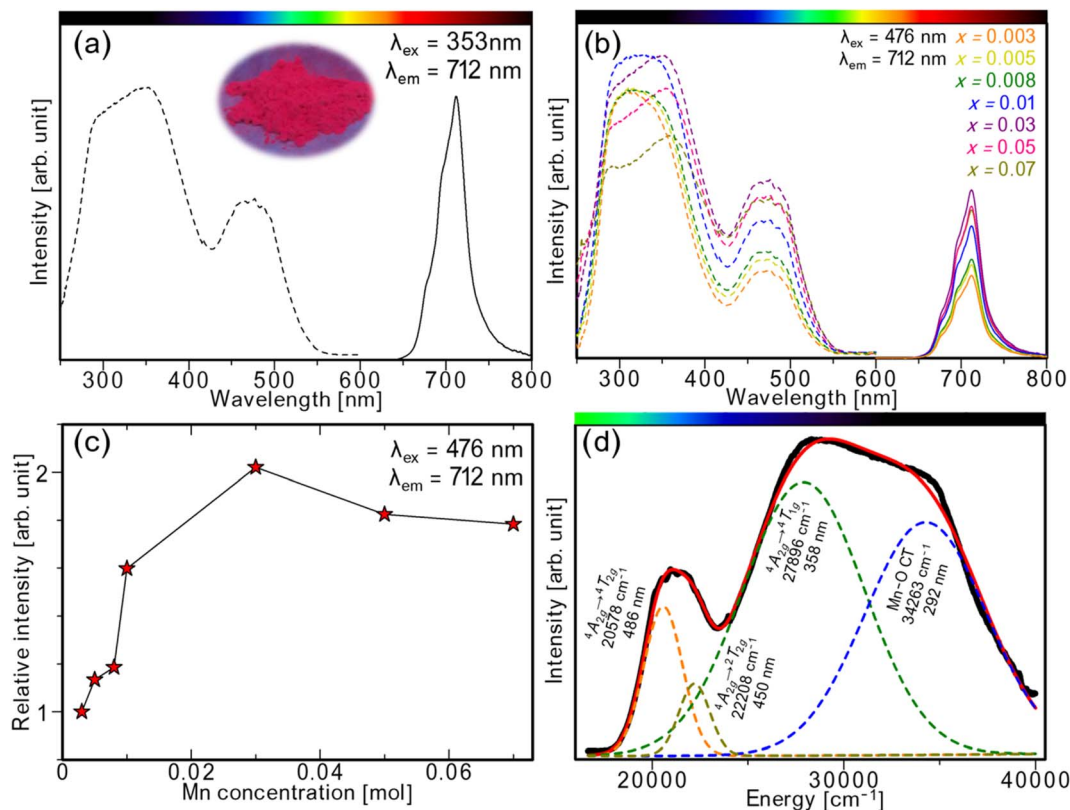Moreover, the average decay lifetimes τ_{ave} are calculated by the following integral decay model (eqn (5));[59]

Fig. 6 (a) PL and PLE spectra of SrCa$_2$Ga$_2$O$_6$:0.03Mn^{4+}. The insert photograph is emission color of SrCa$_2$Ga$_2$O$_6$:0.03Mn^{4+} under 365 nm n-UV irradiation. (b) PL and PLE spectra of SrCa$_2$Ga$_2$O$_6$:xMn^{4+} (0 ≤ x ≤ 0.07) excited at 476 nm. (c) Dependence of emission intensities of SrCa$_2$Ga$_2$O$_6$:Mn^{4+} on the concentration of Mn^{4+} ion. (d) Deconvoluted PLE spectra by four components of Gaussian curves. Red line is fitting curve.

Table 3 Quantum efficiencies of SrCa$_2$Ga$_2$O$_6$:Mn^{4+} and other Mn^{4+}-activated gallate phosphors

Phosphor	IQE	EQE	Ref.
SCG:0.03Mn^{4+}	66%	50%	This study
Ca$_{14}$Zn$_6$Ga$_{10}$O$_{35}$:Mn^{4+}	51%	45%	24
Mg$_7$GeGa$_2$O$_{12}$:Mn^{4+}	28%	—	28
Mg$_3$GeGa$_2$O$_8$:Mn^{4+}	65%	—	30
SrLaGa$_3$O$_7$:Mn^{4+}	14%	—	33
Ca$_7$Mg$_2$Ga$_6$O$_{18}$:Mn^{4+}	51%	—	34

$$\tau_{ave} = \frac{\int_0^\infty tI(t)dt}{\int_0^\infty I(t)dt} \quad (5)$$

The fitting results are listed in Table S5.† The measurement result is reasonable because microsecond-order PL lifetimes are usually observed in Mn^{4+} phosphors.[60] The average lifetime decreases from 2.573 to 2.026 ms with increasing Mn^{4+} concentration, and the shape of decay curves become linear to non-linear. The decreased lifetime and concentration quenching are thought to be caused by nonradiative energy transfer among adjacent Mn^{4+} ions. The nonradiative energy transfer is due to exchange or electric multipole interactions.[61] To determine the origin of the concentration quenching, a critical distance for energy transfer R_c was calculated by an eqn (6);[62]

$$R_c = 2\left[\frac{3V}{4\pi x_c N}\right]^{\frac{1}{3}} \quad (6)$$

where V is the host lattice volume, x_c is a critical concentration of dopant, and N is the number of sites available for the dopant in the unit cell. According to the equation, R_c is determined to be 38.96 Å. The origin of concentration quenching is suggested to be the electric multipole interaction because R_c is much larger than 5 Å.[61] Moreover, to specify the type of electric multipole interaction, the following formula (eqn (7)) was used;[63]

$$\log\left(\frac{I}{x}\right) = A - \left(\frac{\theta}{3}\right)\log x \quad (7)$$

where I is the emission intensity, x is the dopant concentration, A is a constant, and θ is the electric multipole index with $\theta = 3$, 6, 8, and 10 corresponding to nonradiative energy transfer among nearest-neighbor ions, electric dipole–dipole, dipole-quadrupole, and quadrupole–quadrupole interaction, respectively.[64] In the concentration range of $0.03 \leq x \leq 0.07$, the θ is determined to be 2.60, which is close to 3. This fact contradicts the result of R_c calculation, and indicates that considering only Mn^{4+} ions in octahedral sites is not appropriate to discuss the concentration quenching mechanism. According to Liao et al., in the Ca$_{14}$Zn$_6$Ga$_{10}$O$_{35}$:Mn phosphor, doping high amount of Mn^{4+} leads to existence of Mn^{2+} and Mn^{5+} in the host lattice.[64]

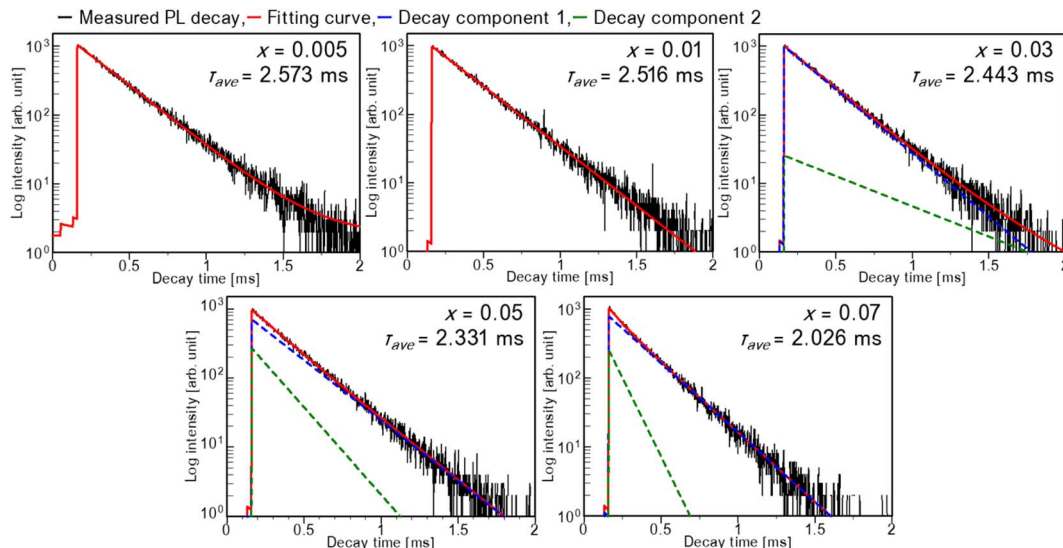**Fig. 7** PL decay curves of $SrCa_2Ga_2O_6{:}x Mn^{4+}$ ($0.005 \leq x \leq 0.07$) monitored at 712 nm excited at 365 nm.

Even in SCG:Mn^{4+} phosphors, the other valent Mn ion behaved as a killer center for Mn^{4+}, and drastic quenching and non-linear rapid lifetime decay were observed in high Mn concentration samples. Therefore, τ_2 are derived from the energy transfer from Mn^{4+} to other valence Mn ions, and the primary concentration quenching mechanism is considered to be that phenomenon. This result is in good agreement with the result of UV-vis diffuse reflectance spectra measurements. Fig. S4† shows the NIR-PL spectra of the SCG:0.03Mn^{4+} phosphor excited by a 568 nm LED light. A characteristic PL spectrum derived from $^1E \rightarrow {}^3A_2$ spin-forbidden transition of tetrahedrally coordinated Mn^{5+} was observed. This fact supports the presence of Mn^{5+} in SCG:Mn^{4+}. In order to increase the luminescence efficiency of SCG:Mn^{4+}, the production of other valence Mn ions should be suppressed.

Crystal field analysis and nephelauxetic effect calculation

The Tanabe–Sugano energy diagram of six-fold octahedral Mn^{4+} ion with a 3 d^3 electronic orbit can be described as Fig. 8. The crystal field strength Dq of Mn^{4+} in the SCG host lattice was calculated by an eqn (8);[32]

$$\mathrm{Dq} = \frac{E\left({}^4A_{2g} \rightarrow {}^4T_{2g}\right)}{10} \tag{8}$$

where $E({}^4A_{2g} \rightarrow {}^4T_{2g})$ is the peak energy of $^4A_{2g} \rightarrow {}^4T_{2g}$ transition (20 578 cm^{-1}). The Racah parameter B is expressed by the following eqn (9);[32]

$$\frac{\mathrm{Dq}}{B} = \frac{15(x-8)}{x^2 - 10x} \tag{9}$$

where x is refined as following eqn (10) using energy gap between $^4A_{2g} \rightarrow {}^4T_{1g}$ and $^4A_{2g} \rightarrow {}^4T_{2g}$ transitions (7318 cm^{-1});[32]

$$x = \frac{E\left({}^4A_{2g} \rightarrow {}^4T_{1g}\right) - E\left({}^4A_{2g} \rightarrow {}^4T_{2g}\right)}{\mathrm{Dq}} \tag{10}$$

Moreover, the Racah parameter C can be represented by an eqn (11) using the peak energy of $^2E_g \rightarrow {}^4A_{2g}$ transition (14 045 cm^{-1});[32]

$$\frac{E\left({}^2E_g \rightarrow {}^4A_{2g}\right)}{B} = \frac{3.05C}{B} + 7.9 - \frac{1.8B}{\mathrm{Dq}} \tag{11}$$

From the above, Dq, B, and C were determined as 2058 cm^{-1}, 707 cm^{-1}, and 2927 cm^{-1}, respectively. The crystal filed is considered as strong when Dq/B ≧ 2.2, and the Dq/B is 2.91. Therefore, Mn^{4+} has a strong crystal field in the SCG crystal lattice.

According to the Tanabe–Sugano energy diagram, the crystal field strength hardly affects the emission energy of Mn^{4+}. As
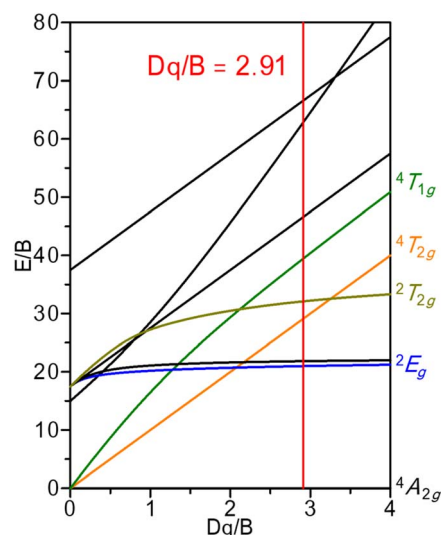

Fig. 8 Tanabe–Sugano energy level diagram of Mn^{4+} at octahedrally coordinated environment. Red line indicates the crystal filed strength of Mn^{4+} in the SrCa$_2$Ga$_2$O$_6$ host lattice.

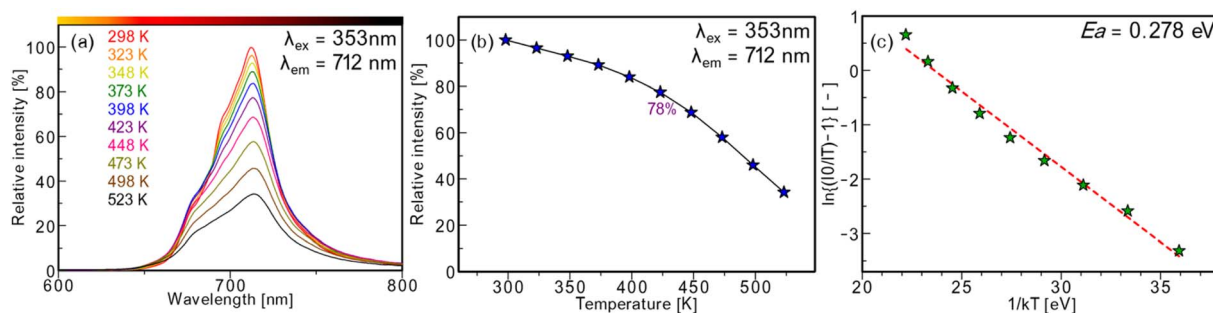**Fig. 9** (a) Temperature-dependent PL spectra of $SrCa_2Ga_2O_6$:0.03Mn^{4+}. (b) The plot of relative emission intensities at each temperature. (c) Arrhenius plot of relative emission intensities for $SrCa_2Ga_2O_6$:0.03Mn^{4+}.

mentioned in the PL properties section, the emission of Mn^{4+} depends on the covalency of center metal and ligands. Therefore, the investigation of the nephelauxetic effect that is derived from chemical bonding is important. The nephelauxetic parameter β_1 is calculated by an eqn (12);[32]

$$\beta_1 = \sqrt{\left(\frac{B}{B_0}\right)^2 + \left(\frac{C}{C_0}\right)^2} \quad (12)$$

where B_0 and C_0 are the Racah parameters of free Mn^{4+} ion, 1160 cm^{-1} and 4303 cm^{-1}, respectively. From the calculation, β_1 was determined to be 0.9133, representing the covalency between Mn^{4+} and ligands is strong.

Thermal quenching properties

The temperature-dependent PL measurement was conducted because the thermal quenching property is an important factor for phosphor applications. The temperature-dependent PL spectra of SCG:0.03Mn^{4+} between 298 K and 598 K are illustrated in Fig. 9a. At 423 K, the relative PL intensity is 78% of that at 298 K. To further study the thermal quenching property, an Arrhenius equation (eqn (13)) was used to calculate an activation energy (E_a);[65]

$$\ln\left(\frac{I_{RT}}{I_T} - 1\right) = \ln A - \frac{E_a}{kT} \quad (13)$$

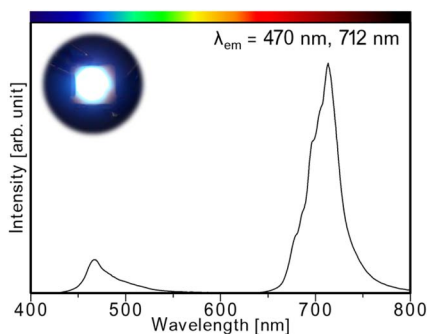where I_{RT} and I_T are the intensities at room temperature (298 K) and arbitrary temperatures, A is a constant, and k is the Boltzmann's constant. Fig. 9(b) and (c) depict PL intensities between 298 K and 598 K and the plot of $\ln[(I_{RT}/I_T) - 1]$ *versus* $1/(kT)$ for SCG:0.03Mn^{4+}. Consequently, the E_a is found to be 0.278 eV. The reported activation energies for $Ca_{14}Zn_6Al_{10}O_{35}$:Mn^{4+} and $Ca_{14}Zn_6Ga_{10}O_{35}$:Mn^{4+} are 0.233 eV and 0.29 eV, respectively, and the activation energy of SCG:Mn^{4+} is found to be close to them.[21,56] The results indicate that SCG:Mn^{4+} has good thermal stability.

LED application

To confirm the potential of SCG:Mn^{4+} as a LED device, a 470 nm blue LED chip and the SCG:0.03Mn^{4+} powder were fabricated into a deep-red emitting LED device. Fig. 10 shows the emission spectrum of the LED device under 10 mA current. The device exhibited two peaks at maxima of 470 and 712 nm, which originated from the blue LED chip and SCG:Mn^{4+}. The result indicates SCG:Mn^{4+} can convert blue light into deep-red light, suggesting the potential of lighting applications.

Conclusion

In summary, the novel deep-red emitting phosphor $SrCa_2Ga_2O_6$:Mn^{4+} was discovered in $Sr_3Ga_2O_6$–$Ca_3Ga_2O_6$ solid solution system and successfully synthesized by the conventional solid-state reaction method for the first time. $SrCa_2Ga_2O_6$:Mn^{4+} was found to have the tululite-related structure belonging to space group $F432$ from the single crystal XRD analysis. Mn ion occupied on the Ga octahedral site, and $SrCa_2Ga_2O_6$:Mn^{4+} single crystals exhibited deep-red emission. From UV-vis diffuse reflectance spectra measurement, the broad absorption band between 220 nm and 550 nm by Mn^{4+} in the six-fold octahedral coordination environment was observed from the $SrCa_2Ga_2O_6$:0.03Mn^{4+} powder. $SrCa_2Ga_2O_6$:Mn^{4+} powders exhibited deep-red emission peaked at 712 nm under the n-UV/blue light. The optimal Mn^{4+} concentration was $x = 0.03$, and the internal and external quantum efficiencies were 66% and 50%. The luminescence lifetime gradually decreased with increasing Mn^{4+} concentration, and the concentration quenching occurred in concentration range of $0.03 \leq x \leq 0.07$. The causal mechanism of concentration quenching was estimated to be energy

Fig. 10 Luminescence spectra of 470 nm blue LED chip packaged with $SrCa_2Ga_2O_6$:0.03Mn^{4+} powder under 10 mA current. The insert photograph is the prepared LED device emitting blue and deep-red light.

transfer from Mn^{4+} to other valence Mn ions. The PL intensity was 78% at 423 K, and the thermal activation energy was calculated as 0.278 eV. The LED device fabricated from the blue LED chip and $SrCa_2Ga_2O_6$:$0.03Mn^{4+}$ powder displayed two emission bands peaked at 470 and 712 nm. Therefore, $SrCa_2Ga_2O_6$:Mn^{4+} was found to have excellent potential as a Mn^{4+}-activated phosphor, and is expected to be used for commercial applications.

Data availability

Crystallographic data for $SrCa_2Ga_{1.87}Mn_{0.13}O_6$ (single crystal) has been deposited at the CCDC under deposition number 2346856.

Conflicts of interest

The authors declare no competing financial interests.

Acknowledgements

References

1 S. Adachi, Photoluminescence properties of Mn^{4+}-activated oxide phosphors for use in white-LED applications: A review, *J. Lumin.*, 2018, **202**, 263–281.

2 X. Wang, O. Li, M. G. Brik, X. Li, L. Li and M. Peng, Thermal quenching of Mn^{4+} luminescence in $SrAl_{12}O_{19}$:Mn^{4+}, *J. Lumin.*, 2019, **206**, 84–90.

3 W. Lü, W. Lv, Q. Zhao, M. Jiao, B. Shao and H. You, A Novel Efficient Mn^{4+} Activated $Ca_{14}Al_{10}Zn_6O_{35}$ Phosphor: Application in Red-Emitting and White LEDs, *Inorg. Chem.*, 2014, **53**, 11985–11990.

4 C. Yang, Z. Zhang, G. Hu, Ru. Cao, X. Liang and W. Xiang, A novel deep red phosphor $Ca_{14}Zn_6Ga_{10}O_{35}$:Mn^{4+} as color converter for warm W-LEDs: Structure, and luminescence properties, *J. Alloys Compd.*, 2017, **694**, 1201–1208.

5 S. P. Singh, M. Kim, W. B. Park, J.-W. Lee and K.-S. Sohn, Discovery of a Red-Emitting $Li_3RbGe_8O_{18}$:Mn^{4+} Phosphor in the Alkali-Germanate System: Structural Determination, and Electronic Calculations, *Inorg. Chem.*, 2016, **55**, 10310–10319.

6 B. Wang, H. Lin, J. Xu, H. Chen and Y. Wang, $CaMg_2Al_{16}O_{27}$:Mn^{4+}-based Red Phosphor: A Potential Color Converter for High-Powered Warm W-LED, *Appl. Mater. Interfaces*, 2014, **6**, 22905–22913.

7 B. Wang, H. Lin, F. Huang, J. Xu, H. Chen, Z. Lin and Y. Wang, Non-Rare-Earth $BaMgAl_{10-2x}O_{17}$:xMn^{4+}, xMg^{2+}: A

8 Narrow-Band Red Phosphor for Use as a High-Power Warm w-LED, *Chem. Mater.*, 2016, **28**, 3515–3524.

8 S. Gu, M. Xia, C. Zhou, Z. Kong, M. S. Molokeev, L. Liu, W.-Y. Wong and Z. Zhou, Red shift properties, crystal filed theory and nephelauxetic effect on Mn^{4+}-doped $SrMgAl_{10-y}Ga_yO_{17}$ red phosphor for plant growth LED light, *Chem. Eng. J.*, 2020, **396**, 125208.

9 R. Cao, Z. Shi, G. Quan, T. Chen, S. Guo, Z. Hu and P. Liu, Preparation and luminescence properties of Li_2MgZrO_4:Mn^{4+} red phosphor for plant growth, *J. Lumin.*, 2017, **188**, 577–581.

10 T. Hasegawa, Y. Nishiwaki, F. Fujishiro, S. Kamei and T. Ueda, Quantitative Determination of the Effective Mn^{4+} Concentration in a Li_2TiO_3:Mn^{4+} Phosphor and Its Effect on the Photoluminescence Efficiency of Deep Red Emission, *ACS Omega*, 2019, **4**, 19856–19862.

11 J. Zhong, D. Chen, S. Yuan, M. Liu, Y. Yuan, Y. Zhu, X. Li and Z. Ji, Tunable Optical Properties and Enhanced Thermal Quenching of Non-Rare-Earth Double-Perovskite $(Ba_{1-x}Sr_x)_2YSbO_6$:Mn^{4+} Red Phosphors Based on Composition Modulation, *Inorg. Chem.*, 2018, **57**, 8978–8987.

12 L. Dang, L. Zhang, Y. Jia, B. Shao, W. Lü, S. Zhao and H. You, Site Occupation and Luminescence of Novel Orange-Red $Ca_3M_2Ge_3O_{12}$:Mn^{2+}, Mn^{4+} (M = Al, Ga) Phosphors, *ACS Sustain. Chem. Eng.*, 2020, **8**, 3357–3366.

13 M. Han, H. Tang, L. Liu, Y. Wang, X. Zhang and L. Lv, Tuning the Mn^{4+} Coordination Environment in Mg_2TiO_4 through a Codoping Strategy for Enhancing Luminescence Performance, *J. Phys. Chem. C*, 2021, **125**, 15687–15695.

14 S. Adachi, Photoluminescence spectra and modeling analysis of Mn^{4+}-activated fluoride phosphors: A review, *J. Lumin.*, 2018, **197**, 119–130.

15 S. Adachi and T. Takahashi, Direct synthesis and properties of K_2SiF_6:Mn^{4+} phosphor by wet chemical etching of Si wafer, *J. Appl. Phys.*, 2008, **104**, 023512.

16 H. Zhu, C. C. Lin, W. Luo, S. Shu, Z. Liu, Y. Liu, J. Kong, E. Ma, Y. Cao, R.-S. Liu and X. Chen, Highly efficient non-rare-earth red emitting phosphor for warm white light-emitting diodes, *Nat. Commun.*, 2014, **5**, 4312.

17 G. Li, X. Shi, X. Lu, Q. Mao, L. Pei, Y. Zhu, M. Liu, L. Chu and J. Zhong, Local Structure Modulation-Induced Highly Efficient Red-Emitting $Ba_2Gd_{1-x}Y_xNbO_6$:Mn^{4+} Phosphors for Warm WLEDs, *Inorg. Chem.*, 2021, **60**, 17398–17406.

18 B. Lan, R. Cao, T. Chen, L. Li, R. Liu, X. Yi, S. Nie and J. Wang, Far-red-emitting $LaSrRO_4$:Mn^{4+} (R = Al and Ga) phosphor: Synthesis and optical properties, *J. Mol. Struct.*, 2022, **1265**, 133484.

19 S. Zhao, J. Xiang, M.-H. Fang, C. Chen, M. Jin and N. Zhang, A novel high thermal stability Ba_2CaWO_6:Mn^{4+} far-red emitting phosphor with a double-perovskite structure for plant growth LEDs, *Opt. Mater.*, 2022, **124**, 112052.

20 S. Adachi, Review—Mn^{4+}-Activated Red and Deep Red-Emitting Phosphors, *ECS J. Solid State Sci. Technol.*, 2020, **9**, 016001.

21 Y. Zhong, S. Gai, M. Xia, S. Gu, Y. Zhang, X. Wu, J. Wang, N. Zhou and Z. Zhou, Enhancing quantum efficiency and tuning photoluminescence properties in far-red-emitting

phosphor $Ca_{14}Ga_{10}Zn_6O_{35}$:Mn^{4+} based on chemical unit engineering, *Chem. Eng. J.*, 2019, **374**, 381–391.

22 Y. Wu, Y. Lv, K. Ruan and Z. Xie, A far-red emission (Ca, Sr)$_{14}Zn_6Ga_{10}O_{35}$:Mn^{4+} phosphor for potential application in plant-growth LEDs, *Dalton Trans.*, 2018, **47**, 15574.

23 T. K. Kuttiat, M. Abraham, A. K. Kunti, N. Amador-Mendez, M. Tchernycheva and S. Das, Enriching the Deep-Red Emission in (Mg, Ba)$_3M_2GeO_8$: Mn^{4+} (M = Al, Ga) Compositions for Light-Emitting Diodes, *Appl. Mater. Interfaces*, 2023, **15**, 7083–7101.

24 Y. Lv, Y. Jin, T. Sun, J. Su, C. Wang, G. Ju, L. Chen and Y. Hu, Visible to NIR down-shifting and NIR to visible upconversion luminescence in $Ca_{14}Zn_6Ga_{10}O_{35}$:Mn^{4+}, Ln^{3+} (Ln = Nd, Yb, Er), *Dyes Pigm.*, 2019, **161**, 137–146.

25 M. Iwaki, K. Uematsu, M. Sato and K. Toda, Structure and Luminescence Studies of a Ce^{3+}-Activated $Ba_5La_3MgAl_3O_{15}$ Green-Emitting Phosphor, *Inorg. Chem.*, 2023, **62**, 1250–1265.

26 S. W. Kim, T. Hasegawa, T. Ishigaki, K. Uematsu, K. Toda and M. Sato, Efficient Red Emission of Blur-Light Excitable new Structure Type $NaMgPO_4$:Eu^{2+} Phosphor, *ECS Solid State Lett.*, 2013, **2**, R49.

27 K. Seki, K. Uematsu, K. Toda and M. Sato, Novel Deep Red Emitting Phosphors $Ca_{14}Zn_6M_{10}O_{35}$:Mn^{4+} (M = Al^{3+} and Ga^{3+}), *Chem. Lett.*, 2014, **43**, 1213–1215.

28 C. Wu, J. Li, H. Xu, J. Wu, J. Zhang, Z. Ci, L. Feng, C. Cao, Z. Zhang and Y. Wang, Preparation, structural and photoluminescence characteristics of novel red emitting $Mg_7Ga_2GeO_{12}$:Mn^{4+} phosphor, *J. Alloys Compd.*, 2015, **646**, 734–740.

29 X. Ding and Y. Wang, Structure and photoluminescence properties of rare-earth free narrow-band red-emitting $Mg_6ZnGeGa_2O_{12}$: Mn^{4+} phosphor excited by NUV light, *Opt. Mater.*, 2017, **64**, 445–452.

30 X. Ding, G. Zhu, W. Geng, Q. Wang and Y. Wang, Rare-Earth-Free High-Efficiency Narrow-Band Red-Emitting $Mg_3Ga_2GeO_8$:Mn^{4+} Phosphor Excited by Near-UV Light for White-Light-Emitting Diodes, *Inorg. Chem.*, 2016, **55**, 154–162.

31 A. M. Srivastava, S. J. Camardello and M. G. Brik, Luminescence of Mn^{4+} in the orthorhombic perovskite, $LaGaO_3$, *J. Lumin.*, 2017, **183**, 437–441.

32 C. Jiang, X. Zhang, J. Wang, Q. Zhao, K.-L. Wong and M. Peng, Synthesis and photoluminescence properties of a novel red phosphor $SrLaGaO_4$:Mn^{4+}, *J. Am. Ceram. Soc.*, 2019, **102**, 1269–1276.

33 Q. Liu, P. Xiong, X. Liu, Y. Fu, S. Wu, Q. Dong, Y. Li, Y. Chen, Z. Ma and M. Peng, Deep red $SrLaGa_3O_7$:Mn^{4+} for near ultraviolet excitation of white light LEDs, *J. Mater. Chem. C*, 2021, **9**, 3969–3977.

34 G. Sivakumar, A. T. Muhammed Munthasir, P. Thilagar and S. Natarajan, Mn-Doped $Ca_{14}Mg_4Ga_{12}O_{36}$ with the Tululite Mineral Structure for Color-Tunable Emission, *Chem. Mater.*, 2024, **36**(11), 5356–5369.

35 M. C. Burla, R. Caliandro, M. Camalli, B. Carrozzini, G. L. Cascarano, L. De Caro, C. Giacovazzo, G. Polidori, D. Siliqi and R. Spagna, IL MILIONE: a suite of computer

36 G. M. Sheldrick, Crystal structure refinement with SHELXL, *Acta Crystallogr., Sect. C:Cryst. Struct. Commun.*, 2015, **71**, 3–8.

37 L. J. Farrugia, WinGX and ORTEP for Windows: an update, *J. Appl. Crystallogr.*, 2012, **45**, 849–854.

38 K. Momma and F. Izumi, VESTA 3 for three-dimensional visualization of crystal, volumetric and morphology data, *J. Appl. Crystallogr.*, 2011, **44**, 1272–1276.

39 F. Izumi and K. Momma, Three-Dimensional Visualization in Powder Diffraction, *Solid State Phenom.*, 2007, **130**, 15–20.

40 H. N. Khoury, E. V. Sokol, S. N. Kokh, Y. V. Seryotkin, E. N. Nigmatulina, S. V. Goryainov, E. V. Belogub and I. D. Clark, Tululite, $Ca_{14}(Fe^{3+}, Al)(Al, Zn, Fe^{3+}, Si, P, Mn, Mg)_{15}O_{36}$: a new Ca zincate-aluminate from combustion metamorphic marbles, central Jordan, *Mineral. Petrol.*, 2016, **110**, 125–140.

41 V. D. Barbanyagre, T. I. Timoshenko, A. M. Ilyinets and V. M. Shamshurov, Calcium aluminozincates of $Ca_xAl_yZn_kO_n$ composition, *Powder Diffr.*, 1997, **12**, 22–26.

42 S. Y. Istomin, S. V. Chernov, E. V. Antipov and Y. A. Dobrovolsky, composition-induced phase transition in $Ca_{14}Zn_{6-x}Ga_{10+x}O_{35+x/2}$ (x = 0.0 and 0.5), *J. Solid State Chem.*, 2007, **180**, 1882–1888.

43 J. Li, J. Huang, P. Jiang, W. Gao, R. Cong and T. Yang, Complex crystal structure and photoluminescence of Bi^{3+}-doped and Bi^{3+}/Eu^{3+} co-doped $Ca_7Mg_2Ga_6O_{18}$, *Dalton Trans.*, 2021, **50**, 6848–6856.

44 J. Grins, S. Y. Istomin, G. Svensson, J. P. Attfield and E. V. Antipov, The disordered cubic structure of $Ca_7Co_3Ga_5O_{18}$, *J. Solid State Chem.*, 2005, **178**, 2197–2204.

45 A. M. Abakumov, J. Hadermann, A. S. Kalyuzhnaya, M. G. Rozova, M. G. Mikheev, G. Van Tendeloo and E. V. Antipov, $Ca_{6.3}Mn_3Ga_{4.4}Al_{1.3}O_{18}$—A novel complex oxide with 3D tetrahedral framework, *J. Solid State Chem.*, 2005, **178**, 3137–3144.

46 A. S. Kalyuzhnaya, A. M. Abakumov, M. G. Rozova, H. D'Hondt, J. Hadermann and E. V. Antipov, Synthesis and crystal structure of the new complex oxide $Ca_7Mn_{2.14}Ga_{5.86}O_{17.93}$, *Russ. Chem. Bull.*, 2010, **59**, 706–711.

47 Q. Zhou, L. Dolgov, A. M. Srivastava, L. Zhou, Z. Wang, J. Shi, M. D. Dramićanin, M. G. Brik and M. Wu, Mn^{2+} and Mn^{4+} Red Phosphors: Synthesis, Luminescence and Applications in WLEDs. A Review, *J. Mater. Chem. C*, 2018, **6**, 2652–2671.

48 P. Li, L. Tan, L. Wang, J. Zheng, M. Peng and Y. Wang, Synthesis, Structure, and Performance of Efficient Red Phosphor $LiNaGe_4O_9$:Mn^{4+} and Its Application in Warm WLEDs, *J. Am. Ceram. Soc.*, 2016, **99**, 2029–2034.

49 M. Peng, X. Yin, P. A. Tanner, M. G. Brik and P. Li, Site Occupancy Preference, Enhancement Mechanism, and Thermal Resistance of Mn^{4+} Red Luminescence in $Sr_4Al_{14}O_{25}$: Mn^{4+} for Warm WLEDs, *Chem. Mater.*, 2015, **27**, 2938–2945.

50 M. Medić, Z. Ristić, S. Kuzman, V. Đorđević, I. Vukoje, M. G. Brik and M. D. Dramićanin, Luminescence of Mn^{4+} activated $Li_4Ti_5O_{12}$, *J. Lumin.*, 2020, **228**, 117646.

51 M. Iwaki, H. Takahashi, K. Uematsu, K. Toda and M. Sato, Emission color shift from green yellow to reddish orange in Eu^{2+}-activated Ca$_6$BaP$_4$O$_{17}$ by doping high amount of activator ion, *J. Lumin.*, 2022, **246**, 118810.

52 X. Ding, Q. Wang and Y. Wang, Rare-earth free red-emitting K$_2$Ge$_4$O$_9$: Mn^{4+} phosphor excited by blue light for warm white-LEDs, *Phys. Chem. Chem. Phys.*, 2016, **18**, 8088–8097.

53 A. M. Srivastava, M. G. Brik, H. A. Comanzo, W. W. Beers, W. E. Cohen and T. Pocock, Spectroscopy of Mn^{4+} in Double Perovskites, La$_2$LiSbO$_6$ and La$_2$MgTiO$_6$: Deep Red Photon Generators for Agriculture LEDs, *ECS J. Solid State Sci. Technol.*, 2018, **7**, R3158–R3162.

54 A. M. Srivastava, H. A. Comanzo, D. J. Smith, J. W. Choi, M. G. Brik, W. W. Beers and S. A. Payne, Spectroscopy of Mn^{4+} in orthorhombic perovskite LaInO$_3$, *J. Lumin.*, 2019, **206**, 398–402.

55 Y. Zhang, C. Zhou, Q. Zhang, P. Yin, X. Sun, K. Wang, J. Wang and X. Feng, Change from La$_2$Ti$_2$O$_7$ to LaTiO$_3$ induced by Li$_2$CO$_3$ addition: Higher local symmetry and particle uniformity achieved an efficient Mn^{4+} activated far red phosphor for agricultural cultivation, *J. Lumin.*, 2022, **248**, 119000.

56 N. Zhou, L. Liu, Z. Zhou, Y. Zhang, M. Li, Z. Zhou, M. Xia and Z. Zhou, Engineering cation vacancies to improve the luminescence properties of Ca$_{14}$Al$_{10}$Zn$_6$O$_{35}$: Mn^{4+} phosphors for LED plant lamp, *J. Am. Ceram. Soc.*, 2019, **103**, 1796–1808.

57 R. Cao, Q. Xiang, W. Luo, D. Wu, F. Xiao and X. Yu, Synthesis and luminescence properties of efficient red phosphors SrAl$_4$O$_7$:Mn^{4+}, R$^+$ (R$^+$ = Li$^+$, Na$^+$, and K$^+$) for white LEDs, *Ceram. Int.*, 2015, **41**, 7191–7196.

58 R. Cao, B. Zhong, J. Nie, L. Zhang, Y. Chen, L. Li, T. Chen and J. Wang, Synthesis, spectral characteristics and energy transfer of SrLa$_2$Al$_2$O$_7$:Mn^{4+}, Dy^{3+}, *J. Lumin.*, 2023, **264**, 120163.

59 W. Sun, Y. Jia, R. Pang, H. Li, T. Ma, D. Li, J. Fu, S. Zhang, L. Jiang and C. Li, Sr$_9$Mg$_{1.5}$(PO$_4$)$_7$:Eu^{2+}: A Novel Broadband Orange-Yellow-Emitting Phosphor for Blue Light-Excited Warm Ehite LEDs, *ACS Appl. Mater. Interfaces*, 2015, **7**, 25219–25226.

60 J. Xiang, J. Chen, N. Zhang, N. Yao and C. Guo, Far red and near infrared double-wavelength emitting phosphor Gd$_2$ZnTiO$_6$:Mn^{4+}, Yb^{3+} for plant cultivation LEDs, *Dyes Pigm.*, 2018, **154**, 257–262.

61 M. D. Dramićanin, B. Milićević, V. Đorđević, Z. Ristić, J. Zhou, D. Milivojević, J. Papan, M. G. Brik, C.-G. Ma, A. M. Srivastava and M. Wu, Li$_2$TiO$_3$:Mn^{4+} Deep-Red Phosphor for the Lifetime-Based Luminescence Thermometry, *ChemistrySelect*, 2019, **4**, 7067–7075.

62 R. Cao, T. Chen, Y. Ren, T. Chen, H. Ao, W. Li and G. Zheng, Synthesis and photoluminescence properties of Ca$_2$LaTaO$_6$:Mn^{4+} phosphor for plant growth LEDs, *J. Alloys Compd.*, 2019, **780**, 749–755.

63 S. Wang, Q. Sun, B. Devakumar, J. Liang, L. Sun and X. Huang, Mn^{4+}-activated Li$_3$Mg$_2$SbO$_6$ as an ultrabright fluoride-free red-emitting phosphor for warm white light-emitting diodes, *RSC Adv.*, 2019, **9**, 3429–3435.

64 Z. Liao, H. Xu, W. Zhao, H. Yang, J. Zhong, H. Zhang, Z. Nie and Z.-K. Zhou, Energy transfer from Mn^{4+} to Mn^{5+} and near infrared emission with wide excitation band in Ca$_{14}$Zn$_6$Ga$_{10}$O$_{35}$:Mn phosphors, *Chem. Eng. J.*, 2020, **395**, 125060.

65 Z. Chen, Z. Tian, J. Zhang, J. Li, S. Du, W. Cui, X. Yuan, K. Chen and G. Liu, Deep-red-emitting Ca$_2$ScSbO$_6$:Mn^{4+} phosphors with a double perovskite structure: Synthesis, characterization and potential in plant growth lighting, *J. Am. Ceram. Soc.*, 2022, **105**, 2094–2104.